PAPER

Check for updates

Synergizing ICP-MS, STEM-EDXS, and SMPS single particle analytics exemplified by superlattice L1$_0$ Pt/Fe aerosol nanoparticles produced by spark ablation†

Vinzent Olszok, ✱[a] Philipp Rembe, [a] Tim Grieb, [b] Eshan J. Wijeyeratnam,[a] Andreas Rosenauer [b] and Alfred P. Weber[a]

Spark ablation was used to continuously synthesize bimetallic L1$_0$ Pt/Fe nanoparticles in an aerosol process involving a furnace and hydrogen as a reducing process gas. For the formation of Pt/Fe in the favorable L1$_0$ crystal configuration, which is a promising electrocatalyst, the Pt–Fe ratio plays a crucial role. State-of-the-art analytics for such multi-element nanoparticles include, among others, electron microscopy (EM) with an element mapping function, such as scanning transmission electron microscopy with energy-dispersive X-ray spectroscopy (STEM-EDXS). Morphological characteristics, local compositions, and element distributions within single particles can be easily derived from EM for a small number of particles. However, a statistical evaluation aiming at the composition of hundreds of single Pt/Fe particles can barely be addressed with such analytics. Driven by the lack of analytical setups aiming at the recording of composition and size distribution of nanoparticles by online diagnostics, this work focuses on a single-particle inductively coupled plasma mass spectrometry (spICP-MS) setup able to resolve this issue. The combination of nanoparticle dilution and classification with spICP-MS allows for the analysis of thousands of multi-element aerosol nanoparticles within minutes. Hence, this article elaborates on the synergy of conducting STEM-EDXS and spICP-MS measurements in parallel, giving the opportunity to multi-dimensionally characterize nanoparticles consisting of more than one element. Beyond metallic particles, the presented setup even allows for the analysis of hetero-aggregated oxidic particles, such as Pt/Fe$_2$O$_3$. Including further offline analytics like X-ray diffraction (XRD), the formation of L1$_0$ Pt/Fe was found to be process gas-dependent and to set in at 400 °C, yielding particles with 56% L1$_0$ content at 1000 °C under a reducing atmosphere.

1 Introduction

Multi-element nanoparticles (NPs), also known as multi-component NPs, nanocomposites, hetero-aggregates or, in special cases, high entropy alloys have attracted much research interest in recent years due to their superior properties relevant for optics,[1] medicine,[2–5] catalysis,[6–8] and even photocatalysis.[9,10] Compared to the manufacturing of multi-element NPs by using, *e.g.*, organometallic precursors, solvents and surfactants, aerosol-assisted approaches appear convenient. In this context, NP production by spark ablation is a promising synthesis technique since ultra-pure metal electrodes and purified

process gases can be used for various combinations of metals, yielding multi-metallic aerosol NPs.[11–16]

One interesting bimetallic material, platinum–iron (Pt/Fe) in L1$_0$ crystal configuration, has until now only been produced by wet-chemical approaches. L1$_0$ Pt/Fe appears to be a promising electrocatalyst with outstanding properties for the oxygen reduction reaction (ORR), making it a valuable material for fuel cells.[17–22] Driven by the lack of simple synthesis routines for such bimetallic catalysts, this work elaborates on a simple and continuous one-step synthesis (spark ablation from metallic electrodes) for such catalyst NPs. However, the synthesis of Pt/Fe in chemically ordered L1$_0$ configuration requires the manufacturer to thoroughly control and maintain a Pt mass fraction of 45–60 wt-% to force Pt/Fe to crystallize in favorable L1$_0$ crystal configuration.[23] This example clearly shows the importance of measuring the achieved composition of produced Pt/Fe NPs. By now, scanning transmission electron microscopy with energy-dispersive X-ray spectroscopy (STEM-EDXS) is a commonly used analytical technique for morphology and composition

[a]Clausthal University of Technology, Institute of Particle Technology, Leibnizstrasse 19, 38678 Clausthal-Zellerfeld, Germany. E-mail: vinzent.olszok@tu-clausthal.de

[b]University of Bremen, Institute of Solid State Physics, Department of Electron Microscopy, Otto-Hahn-Allee 1, 28359 Bremen, Germany

† Electronic supplementary information (ESI) available. See DOI: https://doi.org/10.1039/d4na00276h

elucidation for single-particles. A recent article by Jönsson *et al.* reports that for different binary aerosol NPs (Zn/Cu, Cr/Co, In/Sn, Cu/Ni, Ag/Au, Fe/C, Ni/Ti, Pt/Pd, Fe/Mn, Fe/Cr, Co/Ni) produced by spark ablation, only offline electron microscopy (TEM-EDXS and STEM-EDXS) has been used so far for single-particle composition analysis.[24] They also stated that a low number of analyzed particles may cause larger standard deviations, if single-particle analyses are conducted by (S)TEM-EDXS.

Accompanied by an increasing interest and application of single-particle inductively coupled plasma mass spectrometry (spICP-MS), resulting in a rising number of publications in recent years, this work focusses on utilizing spICP-MS for obtaining composition distributions for multi-element aerosol NPs, which are not available yet for particles produced *via* spark ablation. First attempts of applying ICP devices for aerosol experiments were conducted by Weber *et al.* in the early 1990s for silver NPs using ICP-OES.[25] During the last years, further approaches were reported using spICP-MS for aerosol studies,[26–28] even on hetero-aggregated NPs in waste water[29] and intermetallic NPs.[30,31] In the respective literature, aerosol spICP-MS measurements are often referred to as "DMA-spICP-MS" setups. This nomenclature accounts for a sample introduction *via* an upstream aerosol size classifier unit (differential mobility analyzer, DMA), which directs an aerosol with a predefined particle size into the inductively coupled argon plasma. In this manuscript, the data shown originates from a similar setup. For Pt/Fe aerosol NPs produced by spark ablation, single-particle measurements will be shown, converging in the presentation of composition distributions for bimetallic Pt/Fe and oxidic Pt/Fe_2O_3 particles. The occurrence of oxidic Pt/Fe_2O_3 is, on the other hand, a consequence of utilizing oxidizing process gases (N_2 with residual oxygen) instead of a reducing gas (H_2) for spark ablation, which is mandatory for the formation of oxide-free Pt/Fe in $L1_0$ crystal configuration.

Beyond the presentation of the experimental setup for the synthesis of Pt/Fe NPs and subsequent spICP-MS measurements, this article also gives special attention to temperature-induced morphological changes of Pt/Fe particles, examined by STEM-EDXS. Since spark ablation yields agglomerate-like dendritic particles, post sintering in a reducing gas atmosphere is required for Pt/Fe $L1_0$ formation. As reported in the literature, scanning mobility particle sizer (SMPS) measurements for different sintering temperatures can give useful information regarding the restructuring of multi-element aerosol NPs.[24,32] For this reason, the sintering behavior of Fe and Pt/Fe in two different process gases (N_2 and H_2) will be discussed, ending with a crystallographic assessment by XRD, showing the oxidizing or reducing nature of the process gas to be relevant for the formation of alloyed (Pt/Fe) or segregated (Pt/Fe_2O_3) particles.

2 Particle synthesis, diagnostics and data evaluation

The synthesis of either Pt/Fe or Pt/Fe_2O_3 NPs was performed by means of spark ablation from two opposing metal electrodes at
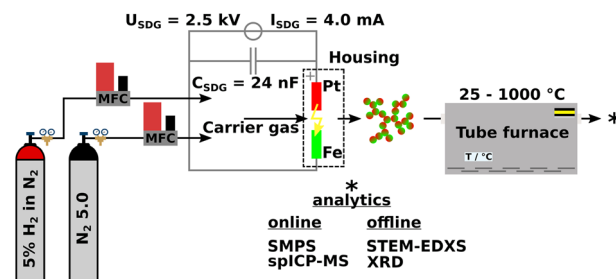

Fig. 1 Experimental setup of the particle synthesis by spark ablation in a spark discharge generator (SDG). The total carrier gas flow rate was kept constant by mass flow controllers (MFC) at 1 L min^{-1}. The residence time of the aerosol within the tube furnace was $\tau_{25\ °C}$ = 21 s. (S)TEM specimen sampling took place at the outlet of the tube furnace by diffusive particle deposition on copper carbon lacey grids with a sample flow rate of 1 L min^{-1} for 2 s.

a breakthrough voltage of 2.5 kV and a charging current of 4 mA. Further parameters are given in Fig. 1. Gasborne particles are formed by the nucleation of metal vapor, which emerges shortly after a spark vaporized solid electrode material. As a consequence, agglomerate-like particles are formed, consisting of multiple primary particles, usually smaller than 10 nm. Further details on spark ablation nanoparticle synthesis, including the dependence of NP size on process parameters such as gas flow rates, *etc.*, are described elsewhere.[33–35] Platinum with a purity of 99.95% was used as an anode material while iron with 99.995% purity was deployed as a cathode (MaTecK Material Technologie & Kristalle GmbH). Both cylindrical electrodes were 3 mm in diameter. The spark discharge frequency was set constant at 40 Hz, even for different process gases such as nitrogen (N_2 5.0, 99.999%, Linde GmbH) or forming gas (5% H_2 in N_2, Linde GmbH) as a reducing atmosphere. Subsequent sintering of freshly generated aerosol particles was conducted in a tube furnace (Nabertherm GmbH), as depicted in Fig. 1.

Online and offline particle analyses were conducted by SMPS (model 3938, TSI Inc.), STEM-EDXS (Thermo Fisher Spectra 300 with a S-CORR probe corrector, an X-FEG, and a SuperX EDXS detector, U = 300 kV), XRD (Empyrean, Malvern Panalytical Ltd, CuK$_\alpha$ λ = 1.5406 Å, PhD$_{low}$ = 8.05 keV, PhD$_{up}$ = 11.27 keV), ICP-MS/MS (8900 triple quad, Agilent Technologies Inc.), and TEM-EDXS (JEM-2100, Jeol, X-Max 80T, Oxford). Particle sampling for offline XRD analytics took place on a track-etched poly-carbonate membrane filter (Sartorius Lab Instruments GmbH & Co. KG) for 1 h. X-ray diffractograms were then recorded with the sample powder placed on a reflex-free monocrystalline silicon wafer. Fig. 2 refers to a schematic of the aerosol NP analysis by spICP-MS as proposed by Bierwirth *et al.*[28] The setup consists of an initial constant aerosol dilution, a size fractioning by an electrostatic classifier (DMA, model 3081A, TSI Inc.), and an adjustable aerosol dilution by a rotating disk diluter (RDD, model 379020A, TSI Inc.) with an eight-cavity disk, which also acts as a gas exchange device, since the spICP-MS device works with argon as a plasma gas. A condensation particle counter (model 3750, TSI Inc.) parallel to the spICP-MS measures the
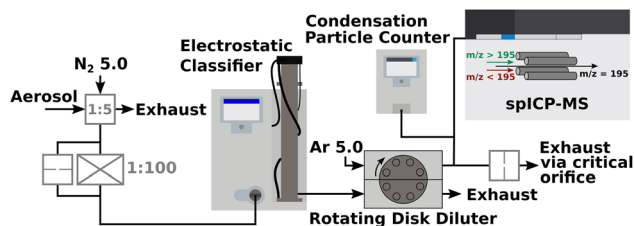
Fig. 2 Interconnection of various aerosol conditioning devices (pre-dilution, classification, gas exchange and dilution, particle concentration measurement) with a spICP-MS device. For the DMA, an aerosol–sheath gas flow ratio of 1 : 20 was set. The RDD was fed with 2 L min^{-1} of argon. 0.9 L min^{-1} and 0.5 L min^{-1} entered the CPC and spICP-MS, respectively. The spICP-MS plasma power was set constant at 1550 W with a reflected power of 2 W. The dwell time was 100 µs as the total acquisition time was 120 s. Platinum was measured at $m/z = 195$ u in no-gas mode for the collision cell.

particle number concentration of the incoming aerosol, which needs to be less or equal to 1 # cm^{-3} to ensure that no coincidence occurs for ICP-MS measurements in single-particle mode. Excess aerosol downstream the RDD gets removed *via* a critical orifice to the exhaust. In this study, spICP-MS measurements were conducted using a gas phase approach, diverging from the standard procedure based on the nebulization of liquid NP suspensions by pneumatic atomizers, positively expressing a significantly reduced background signal.

The acquisition and calculation of the composition distributions (Fig. 5a and b) require the spICP-MS device to be calibrated by aerosol NPs instead of a classical calibration from a particle suspension or an ionic standard solution, since the background signal changes dramatically when either a liquid or a gas carries the analyte. For TiO$_2$ NPs, the aerosol calibration of the spICP-MS device was reported in a recent work[36] but will be discussed briefly with special attention to pure metallic (Pt/Fe) and metal oxide (Pt/Fe$_2$O$_3$) aerosol NPs. First, spherical NPs made of pure platinum were produced by spark ablation and subsequent sintering in a tube furnace at 1300 °C. Downstream the furnace, a DMA classified Pt particles at 20, 30, 40, and 50 nm mobility diameter (d_{Mob}). Thus, a calibration plot can be drawn with the spICP-MS signal in counts-per-second (CPS) over mobility diameter, following a perfect cubic dependency (ICP-MS signal response $\propto m_{Particle} \propto d_{Particle}^3$), see Fig. S1.† Once pure metallic or metal oxide particles containing platinum are directed into the argon plasma of the spICP-MS, the mass of platinum in each particle can be measured, making the whole setup an online single-particle analytical method. From the set mobility diameter at the DMA, the particle volume is known; together with the measured mass of platinum in each particle, the fraction of iron can be easily calculated for pure metallic particles, since only platinum and iron are apparent. One additional step is necessary when metal oxide particles are measured *via* spICP-MS, due to the presence of oxygen contributing to the volume of classified particles. In this case, the difference of the particle volume and the platinum volume yields the volume of Fe$_2$O$_3$. With $v_{Fe} = 2v_{Fe_2O_3} \dfrac{M_{Fe}}{M_{Fe_2O_3}}$, the volume and thus the mass of iron can be calculated for oxidic

particles using the fraction of the molar masses of Fe and Fe$_2$O$_3$. At this point, it is crucial to emphasize that the stoichiometry and the crystal type of the oxidic iron have to be known prior to this calculation. The occurrence of Fe$_2$O$_3$ in oxidic particles will be discussed in detail in the Crystallography section of this manuscript.

The limitation of the spICP-MS setup is given by the smallest detectable particle size, which is in turn dependent on the element under investigation.[37] For Pt, $d_{spICP-MS, min} = 12.8$ nm, according to literature. However, due to the coupling of spICP-MS with an aerosol conditioning and sample introduction system, the above-mentioned smallest detectable particle size might be shifted to even smaller particle sizes, since matrix effects are canceled out by using a gas as a particle carrier instead of, *e.g.*, water.[38]

3   Results and discussion

3.1   Sintering of Pt/Fe agglomerates in oxidizing and reducing atmospheres

From literature it is known that NPs, which appear as agglomerates with a distinct primary particle structure, exhibit an altered sintering behavior when the temperature treatment occurs in either an oxidizing or reducing gas atmosphere.[39,40] For this reason, the sintering behavior of Pt/Fe and Fe agglomerates based on SMPS data will be discussed first, including a primary particle size evaluation for Pt/Fe by TEM imaging. The SMPS measurements aim at the detection of morphological changes in the agglomerate structure towards compact particles as the temperature increases. Electron microscopy focuses on the alteration of primary particles and their size within single agglomerates.

The normalized particle size data shown in Fig. 3a originate from online SMPS scans. As can be seen, the sintering behavior of Pt/Fe is strongly dependent on the chosen process gas. In recent studies, several groups showed nitrogen with 99.999% purity (5.0) to exhibit an oxidizing character for metallic nanoparticles, while small amounts of hydrogen in nitrogen were shown to create a reducing gas atmosphere.[40,41] From this point of view, the green and red curve in Fig. 3a, N$_2$ and H$_2$, respectively, can be explained: hydrogen prevents the iron to form oxides, while residual oxygen in N$_2$ 5.0 boosts the formation of Fe$_2$O$_3$, delaying the sintering progress. Consequently, the green curve lays above the red curve. Note the stronger fluctuating sintering profile of Pt/Fe in an oxidizing atmosphere compared to the reducing gas atmosphere. As will be discussed in the STEM-EDXS section, the variety of morphologies is larger for Pt/Fe$_2$O$_3$ compared to bimetallic Pt/Fe. This non-uniformity of aerosol particles may cause a coarser sintering profile. For comparison purposes, the sintering curve of pure iron agglomerates under N$_2$ 5.0, hence an oxidizing atmosphere, is plotted in Fig. 3a as well (black profile). Two size decrease regimes become observable with a relatively flat, and a steeper section, label ① and ②, with increasing temperature. Iron ($T_{m, Fe} = 1538$ °C) gets easily oxidized by residual oxygen in N$_2$ 5.0 ($c_{O_2} \approx$ 1–5 ppm), which leads to a material with a somewhat higher bulk melting point ($T_{m, Fe_2O_3} = 1565$ °C).
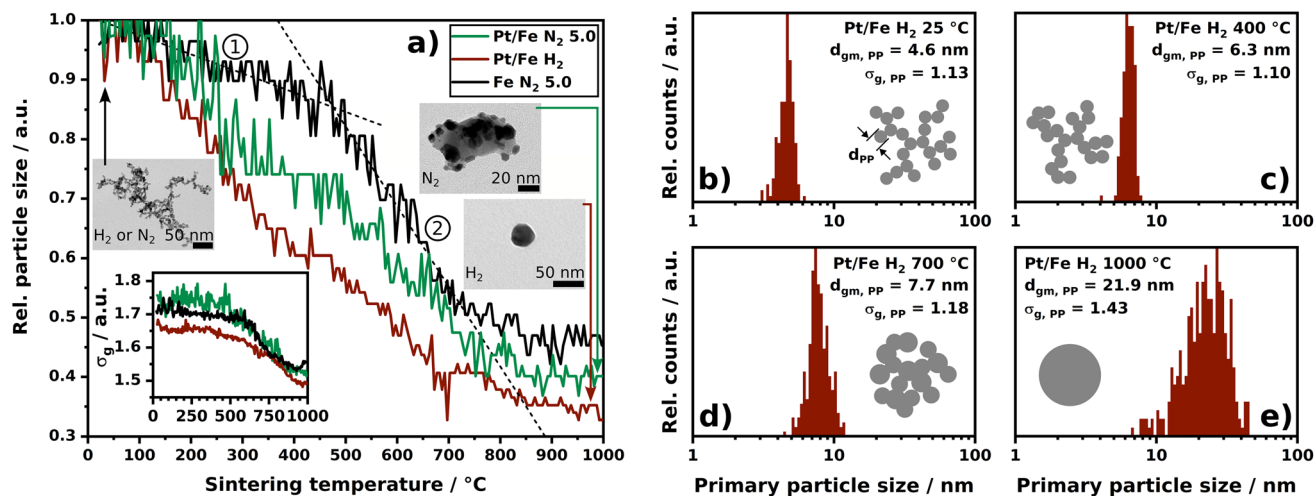
Fig. 3 (a) Normalized particle size (mode) as a function of the sintering temperature. The bottom left inset shows the geometric standard deviation factor σ_g of the particle size distribution at the indicated temperature. The heating ramp from room temperature up to 1000 °C was set constant at 5 K min^{-1}. Every 90 s, a full SMPS scan was conducted. The black dashed lines act as a guide to the eye. TEM micrograph insets show the agglomerate particle morphology to vanish due to temperature treatment. (b–e) Primary particle size distributions for subsequently progressing sintering of Pt/Fe agglomerates under H$_2$ with $d_{gm, PP}$ as the geometric mean diameter of the primary particles and $\sigma_{g, PP}$ as their geometric standard deviation factor. Primary particle size distributions of Pt/Fe agglomerates sintered under N$_2$ are shown in Fig. S2.†

Therefore, a slow sintering seems realistic, as can be confirmed by the shown sintering curve. However, the two observable regimes seem to represent two mechanisms to be relevant for temperature induced agglomerate restructuring. With respect to relevant literature, the first linear size decrease (①) can be explained by an agglomerate compaction where openly structured agglomerates increase their fractal dimension without an increase in primary particle size. The steeper second size drop (②) represents sintering and an accompanying primary particle growth.[42] On the other hand, the sintering curve of Pt/Fe under N$_2$ 5.0 does not show such a characteristic restructuring. In this case, the noble character of platinum, which does not form oxides, contributes to an initial decrease in agglomerate particle size as can be seen in the deviation of the green and black profile up to 700 °C. The idea of an initial restructuring of the agglomerate and a later sintering becomes also observable for Pt/Fe sintered under H$_2$. But in this case, the sintering curve does not show any evidence of such behavior; additional TEM imaging can help address this issue, as can be seen in Fig. 3b–e. The size distributions of the primary particles show clearly that the primary particle size does not change significantly from room temperature up to 400 °C while the sintering curve does show an agglomerate particle size decrease. At 700 °C and 1000 °C, substantially larger primary particle sizes can be found, underlying the two steps, compaction and sintering, to be relevant for the interpretation of sintering curves, not only for single-material NPs.

Since each data point in Fig. 3a represents the mode of a whole particle size distribution (PSD) obtained by SMPS at a certain temperature, the evolution of the geometric standard deviation factor σ_g of each recorded PSD can be discussed as well (inset in Fig. 3a). As can be seen from the nearly unaffected σ_g up to 600 °C of Fe and Pt/Fe under different process gases, a homogenous compaction in all agglomerate size classes can

be assumed, backing the aforementioned size reduction mechanism to involve compaction and subsequent sintering.

3.2 Morphology evaluation by electron microscopy

From online SMPS particle size scans itself, a "state of alloying" or "state of mixing" is not derivable. However, the altered sintering behaviors point at a gas-dependent particle restructuring with increasing temperature, making online SMPS measurements a helpful tool for particle formation elucidation. Morphological information, or even data on the distribution of two distinct elements, e.g. Pt and Fe, cannot be deduced. In this case, high-resolution electron microscopy, coupled with an element mapping function, can provide significant information on multi-element NPs. Since the reduction of surface free energy drives agglomerates to sinter into spheres, which was shown by SMPS, the initial state of mixing of Pt and Fe in room temperature agglomerates and within sintered particles is one of the most interesting questions electron microscopy can address. Fig. 4a–e show STEM-EDXS net peak intensity maps and high-angle annular dark field (HAADF) micrographs of room temperature agglomerates. From Fig. 4a it can be seen that Pt and Fe occur well mixed in every single primary particle. To verify the presence of Pt and Fe in a larger number of particles, Fig. 4b shows an image section with lower magnification. Here it becomes observable that all sampled agglomerates consist of both, Pt and Fe. Nevertheless, to obtain a statistically reliable composition, it would have been necessary to analyze several hundred up to thousands of agglomerates using STEM-EDXS against the background of the error being proportional to $\frac{1}{\sqrt{N}}$. This aspect will be addressed in more detail in the spICP-MS section of this manuscript.

Despite poor statistics, the imaging of room temperature agglomerates yields valuable information about the
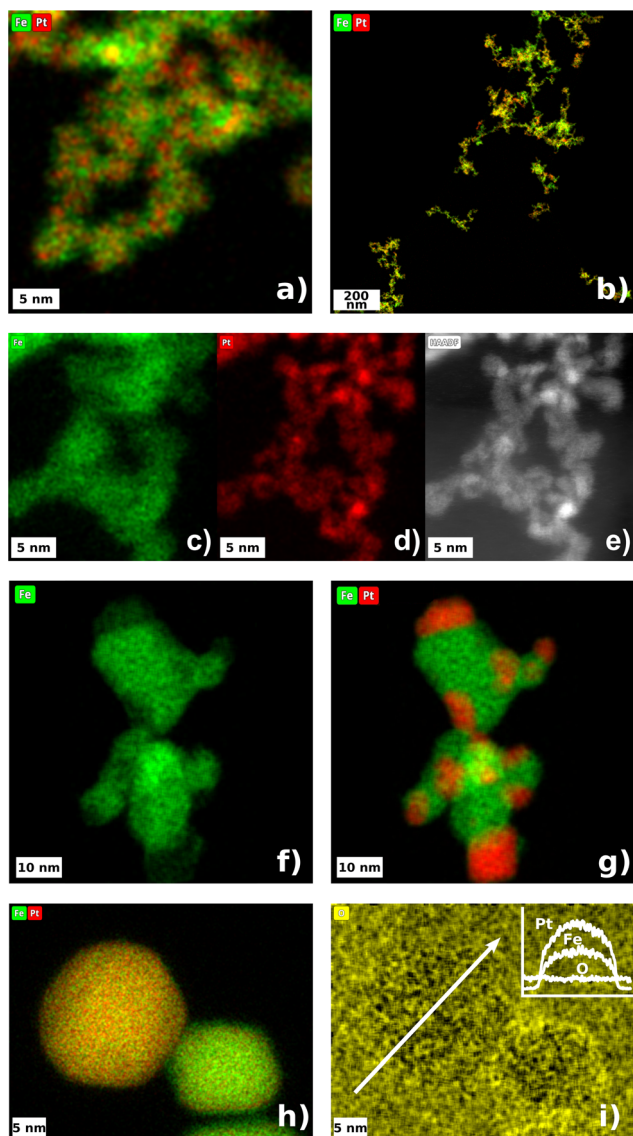
Fig. 4 STEM-EDXS net peak intensity maps and HAADF micrographs of Pt/Fe particles. Color code: green iron, red platinum, yellow oxygen. (a–e) depict the as-synthesized Pt/Fe agglomerates at room temperature. (f and g) show the elemental distribution within a Pt/Fe$_2$O$_3$ particle, which was sintered under N$_2$. (h) shows two Pt/Fe NPs sintered under H$_2$. The larger 22 nm particle contains 75 wt-% Pt, and the smaller 15 nm particle contains 60 wt-% Pt. (i) shows the oxygen map corresponding to (h). The upper right inset displays the EDXS intensities for a line-scan across the 22 nm particle showing a constant oxygen-level. The white arrow indicates the line-scan path.

magic numbers) tend to occur more frequently than clusters with an arbitrary number of atoms not aligned with these magic numbers.[43] Clusters with $N = 1, 13, 55, 147…$ atoms are known to be energetically preferred. For a Pt cluster in a face centered cubic (fcc) crystal with $N = 55$ atoms, the resulting cluster size is 1.39 nm, assuming a lattice constant of 0.392 nm. This cluster size coincides quite significantly with the sub-primary particle size of Pt embedded in Fe, derived from HAADF imaging. The vaporized iron seems to be more stable at comparable time scales, resulting in the creation of a cohesive matrix, surrounding several platinum sub-primary particles. Nevertheless, the match of the presented estimate of a 55-atom cluster with the sub-primary particle size derived from HAADF micrographs could be a coincidence. A more detailed study is advised, aiming at the dependence of the platinum sub-primary particle size on variable synthesis parameters. At this point, however, it is crucial to mention that the elemental distribution of Pt and Fe within room temperature primary particles or whole agglomerates does not depend on the chosen process gas (N$_2$ and H$_2$), which is not explicitly shown here.

Taking Fig. 4f and g into account, the influence of residual oxygen becomes clear. At 1000 °C, the iron, in the form of iron oxide, formed a larger cohesive fundament for segregated Pt adhesions. Differences in the surface energy of Pt and oxidic iron induced a coalescence within the agglomerates and a subsequent movement of Pt towards the surface. For a comparable alloy, Pd/Fe, oxygen was found to induce a segregation of oxidic iron from Pd at 550 K.[44] The direct comparison of Fig. 4f and g with Fig. 4h shows the tremendous impact of the process gas, in this case H$_2$, on the mixture of Pt and Fe at 1000 °C again. Contrary to the particles sintered under N$_2$, the H$_2$ particles seem to appear as a homogenous alloy of Pt and Fe along the whole projection area. Hydrogen as a reducing agent prevents the formation of oxides, enabling the metallic iron to permeate into the platinum crystal. Note the shape of the particles sintered under N$_2$ and H$_2$ (Fig. 4g and h) with a circularity of 62.6 ± 17.6% and 94.1 ± 2.6%, respectively. The Pt/Fe particles have already attained the thermodynamically favorable sphere-like shape, whereas the Pt/Fe$_2$O$_3$ particles exhibit a morphology somewhat deviating from a sphere at 1000 °C. For such particles, a temperature of at least 1450 °C is needed to sinter Pt and Fe$_2$O$_3$ into sphere-like particles with a circularity of 94.9 ± 1.8%, resulting in janus-shaped Pt/Fe$_2$O$_3$ aerosol particles (tested with a high-temperature tube furnace, see Fig. S3†).

The last sub-figure (Fig. 4i) addresses the susceptibility of Pt/Fe particles to oxidation at room temperature. After the particles were produced and sampled, the carbon grid was stored under ambient conditions for several days before the STEM-EDXS analysis was conducted. However, the oxygen map does not show a significant increase in oxygen at the particle's surface compared to the background. This observation agrees with the assumption of the formation of an alloy, where Pt protects the incorporated Fe from oxidation. At moderate temperatures, alloyed Pt/Fe can be seen to be as inert as pure Pt. Note that EDXS mapping of oxygen is a semi-reliable approach to investigate the state of oxidation, since the K$_\alpha$ X-ray quantum energy of oxygen is only 0.5249 keV. Hence, oxygen X-rays are

distribution of two components within one single primary particle. As can be seen in Fig. 4c–e, the platinum seems to form sub-primary particles ("clusters"), 1.55 ± 0.23 nm in diameter, which are embedded in a matrix of Fe. The Pt EDXS scan reveals a coarse structure of such sub-primary particles, which can also be seen in the HAADF micrograph (Fig. 4e). This observation could be explained by a more rapid Pt nucleation after the spark ablated material from the electrodes. During the synthesis of atomic clusters by spark ablation, it is reported that clusters exhibiting a specific number of atoms (referred to as structural
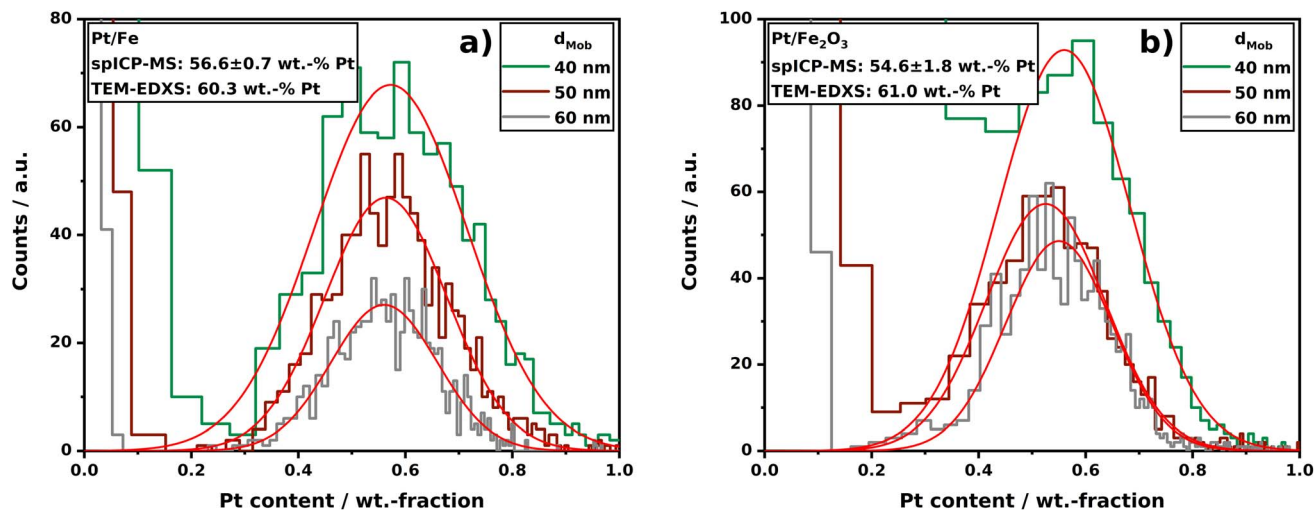
Fig. 5 Composition distributions of Pt/Fe (a) and Pt/Fe$_2$O$_3$ (b) aerosol NPs sintered at 1000 °C obtained by spICP-MS. For each indicated size fraction, $n = 1000 \pm 50$ single-particles were analyzed. The red Gaussian fits act as a guide to the eye. spICP-MS raw data are depicted in Fig. S4 and S5.†

more prone to absorption within the sample material. Specialized analytics would be required for in-depth surface investigations, with options including X-ray Photoelectron Spectroscopy (XPS) for offline analysis or Aerosol Photoemission Spectroscopy (APES) for real-time online analysis.[45]

3.3 Online single-particle composition analysis by spICP-MS

The evaluation of the sintering behavior by SMPS, supported by STEM imaging revealed a process-gas dependent restructuring of Pt/Fe agglomerates with different outcome for nitrogen and hydrogen. Here, the "mixing conditions" of both relevant elements in Pt/Fe NPs could be reliably derived from STEM-EDXS mappings for several single-particles on a carbon grid. However, the question regarding statistical evaluations of the homogeneity of produced particles, with respect to their composition, was already mentioned in the STEM-EDXS section. In the following, composition distributions for both Pt/Fe and Pt/Fe$_2$O$_3$ aerosol NPs will be discussed, which were recorded in a setup, allowing the mass determination of a certain element by spICP-MS. The advantage of this technique is given by the fact that several thousands of single aerosol NPs can be analyzed within a couple of minutes. Compared to an offline evaluation of deposited particles by STEM-EDXS, spICP-MS can significantly boost composition analyses, regarding the time for sample preparation and analysis. In addition, a particle sampling and as a consequence thereof an exposure to ambient air, the spICP-MS setup is a closed and gas-tight system. Thus, produced particles will not get in contact with any other environment than the intended process gas until a dilution with argon upstream the spICP-MS device. Although Pt/Fe was shown to be unaffected by oxygen at room temperature, this fact might be of great importance for other oxygen-affine materials.

Fig. 5a and b show the Pt content in analyzed particles in three different size classes: 40, 50, and 60 nm. The classification was performed by an electrostatic classifier; hence, the given size is a mobility equivalent particle size (d_{Mob}), which in turn

equals a projection area equivalent particle size. From Fig. 5a, a symmetric distribution of Pt in Pt/Fe particles is observable for all three sizes. From the center of the Gaussian fits (red lines in Fig. 5a and b), a mean composition of sintered particles can be derived, which coincides with TEM-EDXS analyses quite well. The data shown also underline that differently sized particles exhibit the same mean composition. From this, it can be stated that smaller and larger initial agglomerates, which consequently sinter into smaller or larger spheres, show the same composition. However, the spICP-MS analysis of particles produced by spark ablation demonstrate that relatively broad but symmetrical composition distributions occur, if multi-element particles are produced by asymmetric spark ablation from two different electrodes. From this it can be assumed that spark ablation from alloyed electrodes would lead to more narrow composition distributions, which was shown for Ag/Au NPs using (S)TEM-EDXS.[24] Nevertheless, the determination of the composition distribution is particularly interesting for multi-element systems that cannot be produced from alloyed electrodes, as certain metals are simply not alloyable. An example is the Ni/Ag system, which can only be produced as NP by spark ablation from two different electrodes.[46]

In Fig. 5b, the Pt content in classified Pt/Fe$_2$O$_3$ particles is displayed. Note that the fraction of oxygen was excluded from the calculations; the shown distribution solely weighs Pt and Fe. Here, a similar mean composition compared to Pt/Fe can be measured but with an increased standard deviation (Pt/Fe 56.6 ± 0.7 wt-% *vs.* Pt/Fe$_2$O$_3$ 54.6 ± 1.8 wt-%). This could be explained by a diminished classification due to a particle morphology deviating from a perfect sphere for sintered Pt/Fe$_2$O$_3$ particles at 1000 °C (see Fig. 4f and g). It is also observable that the signal-to-background separation at $w_{Pt} < 20$ wt-% is less clear for Pt/Fe$_2$O$_3$ compared to Pt/Fe. This can be attributed to the smaller mass of Pt in Pt/Fe$_2$O$_3$ compared to Pt/Fe at the same size, owing to the particle volume contribution of oxygen in Fe$_2$O$_3$. However, Fig. 5b clearly shows spICP-MS to be a powerful analytical method, even for oxidic multi-element

aerosol particles, if the stoichiometry of the metal oxide (derived from XRD) is known. Nevertheless, STEM-EDXS has shown to be a beneficial approach for the analysis of nanocomposites alongside spICP-MS. As demonstrated in Fig. 4f and g (EDXS mapping of Pt/Fe$_2$O$_3$), a segregation of Pt and oxidic iron occurs during sintering. From an area scan, on the one hand, the composition of the shown particle was determined to be 59 wt-% Pt, which coincides with the spICP-MS data shown in Fig. 5b. On the other hand, spICP-MS is not able to give information on, *e.g.*, the composition of the red colored Pt regions in Fig. 4g. The spot scans can show that the segregated Pt still contains 4 wt-% residual Fe. This fact might be of great importance to an intended application of such particles, if local compositions play a crucial role, *e.g.*, for catalytic reactions.

3.4 Crystallography

As already motivated, multi-element particles can outperform traditional materials, consisting of only one component. For an application of such materials, however, the crystallinity can be a central aspect. In the spICP-MS section, in addition, it was highlighted that a crucial aspect involves gaining insight into the oxidation state of the particles under investigation in order to calculate the Pt–Fe ratio in Pt/Fe$_2$O$_3$ NPs. XRD is a widely used and well-established tool for the identification of crystalline phases in a sample. For this reason, an analysis was conducted on Pt/Fe and Pt/Fe$_2$O$_3$ NPs, with the primary goal of discerning the presence of oxides, determining their oxidation states, and identifying the apparent order of Pt and Fe within alloyed particles. Fig. 6a shows the diffractograms corresponding to Pt/Fe agglomerates, synthesized and sintered in an oxidizing atmosphere. At room temperature (25 °C), strong reflexes of Pt can be identified. Taking HAADF data (inset) into account, it can be stated that in room temperature agglomerates, the Pt occurs crystalline as amorphous iron seems to cover the sub-primary Pt particles. As a consequence of sintering at 1000 °C,

the Pt segregates from the iron oxide, which emerges as γ-Fe$_2$O$_3$. The diffractogram corresponding to the sintered particles agree with the micrographs obtained by STEM-EDXS (Fig. 4f and g), showing iron oxide with segregated Pt adhesions.

The evaluation of the SMPS and STEM-EDXS data, on the other hand, revealed a different sintering under H$_2$ with another morphological outcome. The respective diffractograms for Pt/Fe agglomerates sintered under H$_2$ at distinct temperatures are shown in Fig. 6b. At room temperature, no significant differences are observable for N$_2$ and H$_2$ as a process gas. With increasing temperature, however, various remarkable observations can be recorded. First, no oxides seem to form with increasing temperature. The absence of oxides stems from the reducing properties of gaseous H$_2$ at elevated temperatures. Consequently, iron can engage in the creation of intermetallic alloys with platinum, evident in the appearance of distinct reflexes that signify the establishment of a chemically ordered superlattice structure. This structure involves atomic layers of Pt and Fe alternately stacked along the crystal *c* axis.[47] Arrows in Fig. 6b mark those reflexes, which can be assigned to chemically ordered intermetallic Pt/Fe, also known as L1$_0$ Pt/Fe (see reference JCPDS 43-1359, bottom in Fig. 6b). From this diagram, a minimum temperature can be derived, which is necessary for Pt/Fe to crystallize into the L1$_0$ configuration. Here, first reflexes appear between 400 and 700 °C, indicating the occurrence of Pt/Fe in L1$_0$ phase. Exceeding 400 °C, bulk diffusion of Fe atoms contributes significantly to Pt/Fe alloying.[48] Interestingly, as shown by spICP-MS measurements, the produced particles consist of 56.6 wt-% Pt, favorable for L1$_0$ Pt/Fe formation, as shown by Yu *et al.*[23] These authors found a Pt content of 45–60 wt-% to be beneficial to synthesize L1$_0$ Pt/Fe. Otherwise, the alloy can appear in the chemically unordered fcc structure as a dominating crystal phase. Yu *et al.* also reported a peak shift from 40.5° to 41.4° to occur for the Pt/Fe [111] peak, evidencing the formation of Pt/Fe in L1$_0$ structure. From Fig. 6b, a peak shift from 40.6° to 41.4° is also perceptible with
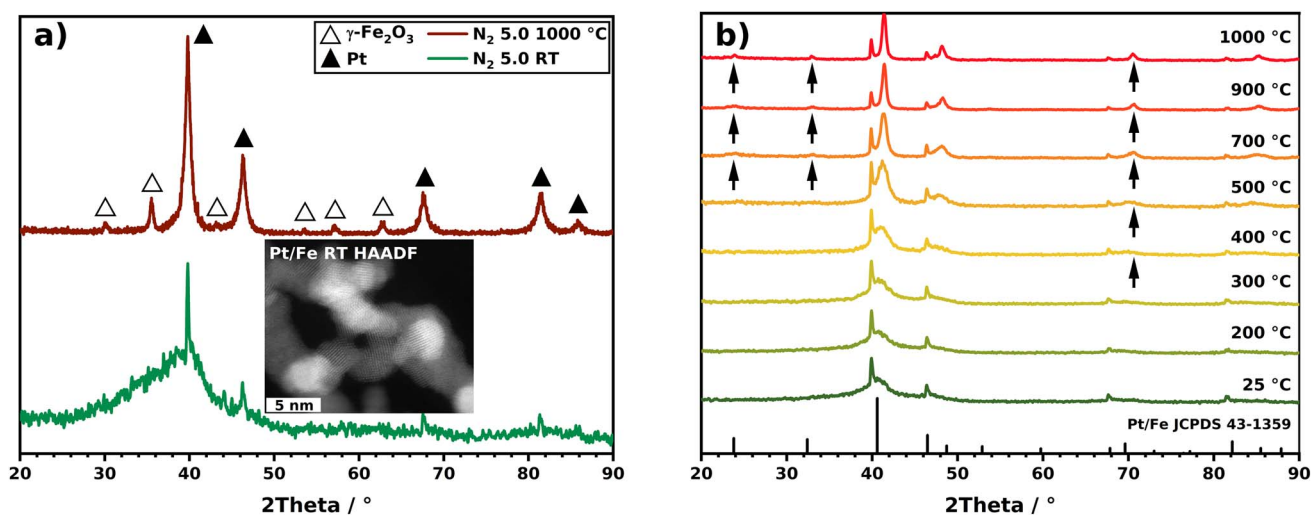

Fig. 6 X-ray diffractograms of (a) Pt/Fe at room temperature (RT) and sintered under N$_2$ at 1000 °C. The inset shows the HAADF image of Pt/Fe NPs at room temperature indicating the crystalline structure of Pt in primary particles. (b) Pt/Fe sintered under H$_2$ at different temperatures. Reference reflexes are given for Pt/Fe in L1$_0$ configuration and additionally indicated by arrows.

increasing temperature (for more details, see Fig. S6†). According to Rong *et al.*, an order parameter β_{L1_0} (eqn (1)) can be defined, which relates to the content of the desired $L1_0$ phase by putting two reflex intensities in relation.[49] For the sintered NPs at 1000 °C, an $L1_0$ content of 56% can be derived.

$$\beta_{L1_0} = 0.85 \sqrt{\frac{I_{24°}}{I_{48°}}} \tag{1}$$

Since XRD investigations require particles to be deposited (here on a polycarbonate filter), further offline techniques, such as BET, TGA, SEM, XPS/AES/UPS *etc.*, can be applied to the sampled particles if more specific information is needed. The whole particle sampling unit, *e.g.* the sealed and gas-tight filter housing, could also be transferred to a glove box where additional sample preparation can be conducted, accounting for subsequent analyses of oxygen-sensitive materials like pure iron NPs.[50] For experiments aiming at, *e.g.*, the catalytic behavior of the product, particles can be easily scratched off of the filter in a controlled environment. The powder could then be used for follow-up studies aiming at the functionality of synthesized NPs.

4   Conclusion

In this work, we present spark ablation as a simple and continuous one-step synthesis method for the production of $L1_0$ Pt/Fe NPs, which are known to be a promising electrocatalyst for the oxygen reduction reaction. The option of using ultra-pure metal electrodes and preconditioned process gases makes spark ablation a robust and reliable synthesis approach for multi-element particle production. Deploying metallic Pt and Fe electrodes in the spark discharge generator, the synthesis yields either bimetallic $L1_0$ Pt/Fe or oxidic Pt/Fe_2O_3 NPs, depending on the chosen process gas. The reducing nature of hydrogen initiates the formation of alloyed Pt/Fe while residual oxygen in nitrogen causes the iron to form oxides during temperature treatment. Since the ratio of Pt and Fe is crucial for the formation of chemically ordered Pt/Fe in the $L1_0$ configuration, a detailed analysis of the composition was addressed in this manuscript. By introducing spICP-MS as an online analytical method for the recording of composition distributions, thousands of Pt/Fe single-particles could be analyzed within a couple of minutes. With this approach, the Pt content in 30, 40, and 50 nm Pt/Fe NPs, produced by spark ablation, was found to be 56.6 ± 0.7 wt-%, ideal for $L1_0$ Pt/Fe formation. A classical way to obtain compositions for single NPs is STEM-EDXS, which was also used as an offline technique in this study. By combining two powerful analytics, spICP-MS and STEM-EDXS, the main drawbacks of one method could be overcome by involving the other analytical method in the particle analysis. Consequently, we were able to provide statistically robust composition distributions for NPs synthesized by spark ablation in an aerosol by spICP-MS for the first time, while STEM-EDXS imaging offered insights into particle morphology, element distributions, and local compositions within single-particles. Coupled with the evaluation of the sintering behavior by SMPS measurements

and a crystallographic assessment by XRD, we found hydrogen to enable the formation of $L1_0$ Pt/Fe starting at 400–700 °C. At 1000 °C, an $L1_0$ phase content of 56% was found. With this article, in conclusion, we proved the effectiveness and reasonableness of combining two online (SMPS and spICP-MS) with two offline analytical methods (STEM-EDXS and XRD) in order to analyze multi-element aerosol NPs multidimensionally. The shown procedures and methods can be applied straight forward to more complex multi-element NPs, enabling a comprehensive characterization of high-performance materials in the future.

Conflicts of interest

The authors declare no conflict of interest.

Acknowledgements

References

1 D. A. Garfinkel, G. Pakeltis, N. Tang, I. N. Ivanov, J. D. Fowlkes, D. A. Gilbert and P. D. Rack, *ACS Omega*, 2020, **5**, 19285–19292.

2 S. Mureed, S. Naz, A. Haider, A. Raza, A. Ul-Hamid, J. Haider, M. Ikram, R. Ghaffar, M. Irshad, A. Ghaffar and A. Saeed, *Nanoscale Res. Lett.*, 2021, **16**, 91.

3 A. L. Padilla-Cruz, J. A. Garza-Cervantes, X. G. Vasto-Anzaldo, G. García-Rivas, A. León-Buitimea and J. R. Morones-Ramírez, *Sci. Rep.*, 2021, **11**, 1–10.

4 M. Pietrzak and P. Ivanova, *Sens. Actuators, B*, 2021, **336**, 129736.

5 D. Wei, X. Zhang, B. Chen and K. Zeng, *Anal. Chim. Acta*, 2020, **1126**, 106–113.

6 X. Fan, Z. Liu, Y. A. Zhu, G. Tong, J. Zhang, C. Engelbrekt, J. Ulstrup, K. Zhu and X. Zhou, *J. Catal.*, 2015, **330**, 106–119.

7 Y. Turap, I. Wang, T. Fu, Y. Wu, Y. Wang and W. Wang, *Int. J. Hydrogen Energy*, 2020, **45**, 6538–6548.

8 M. Yusuf, A. S. Farooqi, L. K. Keong, K. Hellgardt and B. Abdullah, *Chem. Eng. Sci.*, 2021, **229**, 116072.

9 C. Han, L. Wu, L. Ge, Y. Li and Z. Zhao, *Carbon*, 2015, **92**, 31–40.

10 Y.-H. Li, J.-Y. Li and Y.-J. Xu, *EnergyChem*, 2021, **3**, 100047.

11 A. Muntean, M. Wagner, J. Meyer and M. Seipenbusch, *J. Nanopart. Res.*, 2016, **18**, 229.

12 A. Kohut, L. P. Villy, A. Kéri, Á. Bélteki, D. Megyeri, B. Hopp, G. Galbács and Z. Geretovszky, *Sci. Rep.*, 2021, **11**, 1–10.

13 L. P. Villy, A. Kohut, A. Kéri, Á. Bélteki, G. Radnóczi, Z. Fogarassy, G. Z. Radnóczi, G. Galbács and Z. Geretovszky, *Sci. Rep.*, 2022, **12**, 1–9.

14 C. Bulbucan, C. Preger, A. Kostanyan, K. M. Ø. Jensen, E. Kokkonen, C. Piamonteze, M. E. Messing and R. Westerström, *Nanoscale*, 2021, **13**, 15844–15852.

15 P. Pál, V. Horváth, L. Juhász, Z. Kóródi, A. Kohut and I. Csarnovics, *Chemosensors*, 2023, **11**, 180.

16 K. C. Petallidou, P. Ternero, M. E. Messing, A. Schmidt-Ott and G. Biskos, *Nanoscale Adv.*, 2023, **5**, 6880–6886.

17 H. Kuroki, T. Tamaki, M. Matsumoto, M. Arao, Y. Takahashi, H. Imai, Y. Kitamoto and T. Yamaguchi, *ACS Appl. Energy Mater.*, 2018, **1**, 324–330.

18 H. Kuroki, T. Tamaki, M. Matsumoto, M. Arao, K. Kubobuchi, H. Imai and T. Yamaguchi, *Ind. Eng. Chem. Res.*, 2016, **55**, 11458–11466.

19 H. Kuroki, T. Tamaki and T. Yamaguchi, *J. Electrochem. Soc.*, 2016, **163**, F927–F932.

20 S. He, Y. Liu, H. Zhan and L. Guan, *ACS Catal.*, 2021, **11**, 9355–9365.

21 J. Guan, J. Zhang, X. Wang, Z. Zhang and F. Wang, *Adv. Mater.*, 2023, **35**, 1–6.

22 H. Kuroki, T. Yamaguchi, Y. Imura, R. Fujita and T. Tamaki, *ACS Appl. Nano Mater.*, 2020, **3**, 9912–9923.

23 J. Yu, W. Gao, F. Liu, Y. Ju, F. Zhao, Z. Yang, X. Chu, S. Che and Y. Hou, *Sci. China Mater.*, 2018, **61**, 961–968.

24 L. Jönsson, M. Snellman, A. C. Eriksson, M. Kåredal, R. Wallenberg, S. Blomberg, A. Kohut, L. Hartman and M. E. Messing, *J. Aerosol Sci.*, 2024, **177**, 106333.

25 A. P. Weber, R. Keil, L. Tobler and U. Baltensperger, *Anal. Chem.*, 1992, **64**, 672–677.

26 A. Hess, M. Tarik and C. Ludwig, *J. Aerosol Sci.*, 2015, **88**, 109–118.

27 T. Cen, L. Torrent, A. Testino and C. Ludwig, *J. Aerosol Sci.*, 2024, **175**, 106283.

28 M. Bierwirth, V. Olszok, A. Wollmann and A. P. Weber, *J. Aerosol Sci.*, 2022, **163**, 105983.

29 Y. C. Hsieh, Y. P. Lin, T. C. Hsiao and W. C. Hou, *Sci. Total Environ.*, 2022, **838**, 156444.

30 X. Tian, H. Jiang, L. Hu, M. Wang, W. Cui, J. Shi, G. Liu, Y. Yin, Y. Cai and G. Jiang, *TrAC, Trends Anal. Chem.*, 2022, **157**, 116746.

31 Z. Meng, L. Zheng, H. Fang, P. Yang, B. Wang, L. Li, M. Wang and W. Feng, *Processes*, 2023, **11**, 1237.

32 P. Ternero, M. Sedrpooshan, D. Wahlqvist, B. O. Meuller, M. Ek, J. Hübner, R. Westerström and M. E. Messing, *J. Aerosol Sci.*, 2023, 106146.

33 N. S. Tabrizi, M. Ullmann, V. A. Vons, U. Lafont and A. Schmidt-Ott, *J. Nanopart. Res.*, 2009, **11**, 315–332.

34 J. Feng, G. Biskos and A. Schmidt-Ott, *Sci. Rep.*, 2015, **5**, 1–9.

35 T. V. Pfeiffer, J. Feng and A. Schmidt-Ott, *Adv. Powder Technol.*, 2014, **25**, 56–70.

36 J. Poostforooshan, S. Belbekhouche, V. Olszok, M. F. B. Stodt, M. Simmler, M. Bierwirth, H. Nirschl, J. Kiefer, U. Fritsching and A. P. Weber, *ACS Appl. Nano Mater.*, 2023, **6**, 22660–22672.

37 S. Lee, X. Bi, R. B. Reed, J. F. Ranville, P. Herckes and P. Westerhoff, *Environ. Sci. Technol.*, 2014, **48**, 10291–10300.

38 B. Meermann and V. Nischwitz, *J. Anal. At. Spectrom.*, 2018, **33**, 1432–1468.

39 V. Olszok, M. Bierwirth and A. P. Weber, *Nanomaterials*, 2021, **11**, 2266.

40 R. T. Hallberg, L. Ludvigsson, C. Preger, B. O. Meuller, K. A. Dick and M. E. Messing, *Aerosol Sci. Technol.*, 2018, **52**, 347–358.

41 V. Olszok, M. Bierwirth and A. P. Weber, *ACS Appl. Nano Mater.*, 2023, **6**, 1660–1666.

42 K. Nakaso, M. Shimada, K. Okuyama and K. Deppert, *J. Aerosol Sci.*, 2002, **33**, 1061–1074.

43 A. Maisser, K. Barmpounis, M. B. Attoui, G. Biskos and A. Schmidt-Ott, *Aerosol Sci. Technol.*, 2015, **49**, 886–894.

44 Y. Li, B. Yang, M. Xia, F. Yang and X. Bao, *Appl. Surf. Sci.*, 2020, **525**, 146484.

45 V. Olszok, P. Rembe and A. P. Weber, *Aerosol Sci. Technol.*, 2024, **58**, 54–69.

46 M. Gaudry, E. Cottancin, M. Pellarin, J. Lermé, L. Arnaud, J. R. Huntzinger, J. L. Vialle, M. Broyer, J. L. Rousset, M. Treilleux and P. Mélinon, *Phys. Rev. B*, 2003, **67**, 155409.

47 S. Ayaz Khan, P. Blaha, H. Ebert, J. Minár and O. Šipr, *Phys. Rev. B*, 2016, **94**, 144436.

48 H. Chen, R. Wang, R. Huang, C. Zhao, Y. Li, Z. Gong, Y. Yao, Y. Cui, F. Yang and X. Bao, *J. Phys. Chem. C*, 2019, **123**, 17225–17231.

49 C. -B. Rong, D. Li, V. Nandwana, N. Poudyal, Y. Ding, Z. L. Wang, H. Zeng and J. P. Liu, *Adv. Mater.*, 2006, **18**, 2984–2988.

50 T. Rosenberger, I. Skenderović, J. Sellmann, P. Wollny, A. Levish, I. Wlokas, A. Kempf, M. Winterer and F. E. Kruis, *Aerosol Sci. Technol.*, 2022, **56**, 833–846.